

# Energy Filtered Magnetic Induction Mapping

J. DOOLEY and M. DE GRAEF\*

Department of Materials Science and Engineering, Carnegie Mellon University, Pittsburgh PA 15213-3890, U.S.A.

(Received 24 February 1997; revised 30 June 1997)

Abstract—We have implemented an energy-filtered magnetic induction mapping technique on a JEOL 4000EX equipped with a Gatan Imaging Filter. We present an example application of the technique to the study of the magnetic domain structure in Terfenol-D, a magnetostrictive actuator material. The method is equivalent to Differential Phase Contrast microscopy by the reciprocity theorem. To support the observations we have also implemented an image simulation algorithm which permits direct computation of all stages of the induction mapping process. © 1997 Elsevier Science Ltd. All rights reserved

Key words: energy filtered imaging, Lorentz microscopy, magnetic induction mapping, Terfenol-D.

## INTRODUCTION

The study of the domain structure of magnetic materials has for several decades made use of Lorentz microscopy techniques, with Fresnel and Foucault as the most commonly used observation modes (e.g. Reimer, 1993). Virtually all engineering parameters of materials (coercivity, magnetostrictive coefficients, etc.) are directly affected by microstructural features. For instance, the coercivity of Terfenol-D (Tb<sub>0.73</sub>Dy<sub>0.27</sub>Fe<sub>1.95</sub>), used as an actuator material in sonar applications, is strongly linked to the presence of Widmanstätten REFe<sub>3</sub> particles (Lord et al., 1982) which pin the domain walls. The density of these pinning centers can be varied by slightly altering the processing conditions and/or melt composition. Another example is the class of Sm<sub>2</sub>Co<sub>17</sub> based hard magnets, where the presence of Cu-rich or Ga-rich second phase regions, bounding the rhombohedral cells, determines the domain wall mobility and hence the coercivity (Huang et al., 1994).

The decreasing length scale of modern electronic and magnetic devices must be accompanied by improvements in the observation techniques used to study their micro- and nanostructures. Conventional Lorentz microscopy suffers from a reduced final image magnification as compared to conventional transmission electron microscopy, caused by the need for a low-field sample environment and the consequent increase in the focal length of the objective lens. This is a serious limitation for the quantitative study of nanoscale magnetic structures. Furthermore, inelastic scattering in the sample causes an overall blurring of the images, which further limits the attainable resolution of the standard Lorentz modes.

The ultimate goal of micromagnetic observations is to fully document the magnetic induction as a function of location in the sample. This includes a study of domain configurations and the character of the domain walls. There are very few techniques capable of producing direct maps of the (in-plane) magnetic induction in a thin foil. Differential Phase Contrast (DPC) microscopy in a STEM (Chapman et al., 1978) is perhaps the most successful method, but it requires instrument modifications (installation of de-scanning coils and a fourquadrant detector) and is not generally accessible in an average research laboratory. Daykin and Petford-Long (1995) have recently proposed an equivalent technique for the TEM (equivalent to DPC by the reciprocity theorem). They have demonstrated that for thin foils a TEM equipped with a low-field Lorentz pole piece can be used to obtain maps of the components of magnetic induction at right angles to the trajectories of the incident electrons (which, for brevity, we will refer to as the in-plane components). They also point out that inelastic scattering limits the resolution of DPC images in both STEM and TEM so that any form of inelastic scattering filter is desirable.

We have recently reported a novel Lorentz microscopy setup, combining a high resolution top-entry JEOL 4000EX TEM with a post-column Gatan imaging filter (GIF) [Dooley and De Graef, 1997]. When the main objective lens in this microscope is turned off, the sample can be mounted in an essentially field-free region. The objective minilens then provides sufficient field strength to focus the electrons into a diffraction pattern at the selected area (SA) aperture plane. Fresnel and Foucault modes are available by changing the minilens current and moving the SA aperture, respectively. The GIF is used for two purposes: (1) it provides an additional magnification of approximately 20 ×; and (2) it allows for the acquisition of zero-loss images, increasing the signal-to-noise ratio by at least an order of magnitude (Dooley and De Graef, 1997).

We have adapted the induction mapping technique reported by Daykin and Petford-Long (1995) for the 4000EX+GIF combination and in this paper we report on the implementation of the mapping technique, we provide an example of a zero-loss magnetic induction

<sup>\*</sup>Corresponding author.

map for Terfenol-D, and we conclude with a section on the numerical simulation of zero-loss magnetic induction mapping experiments.

### MATERIALS AND METHODS

# Terfenol-D

All experimental images in this paper were obtained from a thin foil of Terfenol-D, or Tb<sub>0.73</sub>Dy<sub>0.27</sub>Fe<sub>1.95</sub>. This material has a cubic Laves phase structure, isomorphous with MgCu<sub>2</sub> (space group Fd3m, Pearson symbol cF24, Struktur Bericht notation C15), with a lattice parameter a=0.732 nm (Al-Jiboory and Lord, 1990). Terfenol-D has a room temperature magnetostriction coefficient  $\lambda_{111} \approx 2200$  ppm, which makes it a material well suited to low-frequency, high power sonar applications. Single crystal rods of Terfenol-D with [211] growth direction (free-standing floating zone method) were obtained from Etrema, and oriented by means of reflection Laue diffraction. Disks with [011] foil normal were cut from [211] oriented rods. Foils were mechanically polished to a thickness of less than 200  $\mu$ m and then jet thinned to perforation in a chilled solution of 10% perchloric/90% acetic acid. Samples were then ion milled for several hours with 4.5 kV Ar<sup>+</sup> ions until electron transparent; prior to microscopy observations, the foils were again ion milled for a short time in order to minimize the thickness of the native oxide layer.

For a detailed description of the microstructure of this material we refer to Lord et al. (1982), James and Kinderlehrer (1993), and Dooley and De Graef (1997). For the purposes of this paper it will be sufficient to state that Terfenol-D, at room temperature, has the (111) directions as soft magnetic directions, resulting in the presence of eight different magnetic induction directions in an un-poled sample. During single crystal growth, 180° rotational growth twins are formed on the (111) plane, resulting in an additional six induction directions. Domain walls are either of the zig-zag 180° type, or the 71° (109°) type, which is the angle between cubic (111) directions. James and Kinderlehrer (1993) have shown that the micromagnetic structure consists of lamellar sequences of alternating domains, intersected by 180° domain walls. Figure 1 shows a Foucault image of one such characteristic lamellar domain arrangement, with the domain wall character indicated on the figure. We will use this area of the sample throughout the paper to illustrate the magnetic induction mapping technique. A comparable domain arrangement will be used as the input structure for simulations of the induction mapping technique.

# Magnetic induction mapping in the TEM

The DPC technique in the STEM requires the addition of a quadrant detector and post-specimen descan coils. In the absence of an in-plane component of

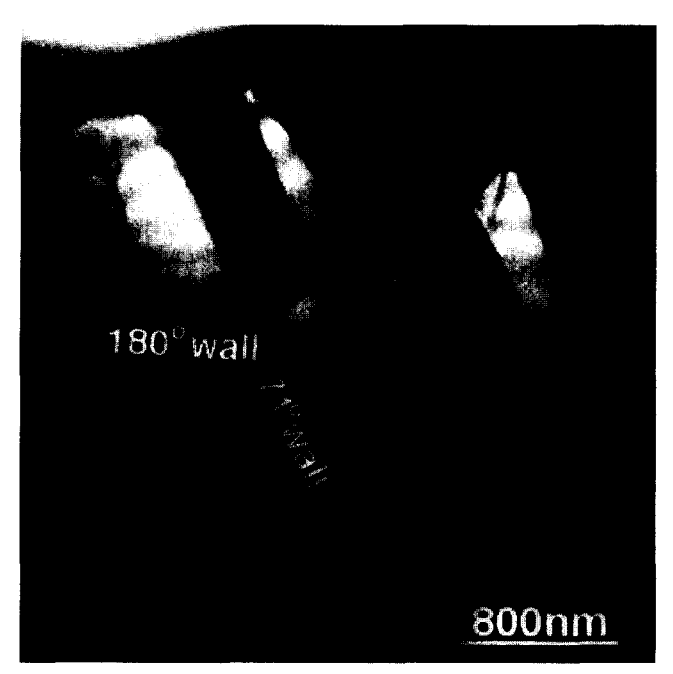
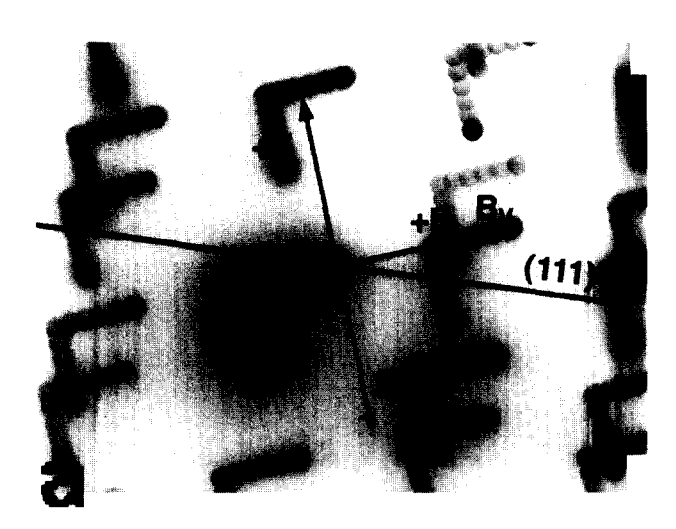


Fig. 1. Zero-loss Foucault image of a Terfenol region in near-[011] orientation, taken with a 15 eV wide slit.

magnetic induction the descan coils maintain the position of the electron beam at the center of the detector, regardless of the position of the probe on the specimen. For a specimen with in-plane magnetic induction components, the additional Lorentz deflection is not compensated for by the descan coils, and hence the beam will move off the center of the detector. The difference currents between the four quadrants of the detector are proportional to the components of the magnetic induction in two orthogonal directions (which we shall represent by the symbols  $\pm U$  and  $\pm V$ ). In this way, the in-plane components of magnetic induction can be measured at a single point, and by scanning the probe over the sample, a two-dimensional map is produced. This technique allows for the direct determination of domain wall profiles, limited in resolution primarily by the probe diameter.

Magnetic induction mapping in the TEM is accomplished by extending the Foucault mode. The method described in this paragraph is based on the method proposed by Daykin and Petford-Long (1995). A converged incident beam, with beam divergence angle  $\theta_0$ , is used to illuminate the region of interest on the sample. A small aperture (small with respect to the diameter of the diffraction disk) is placed in the back focal plane of the objective lens. The electron beam is then tilted after the sample so that the diffraction disk is translated over the aperture. If the beam tilt is imposed in two orthogonal directions, a series of Foucault images is obtained at increasingly larger beam tilt angles. Since each point in the diffraction disk corresponds to an incident beam direction, one effectively samples the incident cone along four different directions  $\pm U$  and  $\pm V$ . Tilting the beam with a fixed aperture is equivalent to detecting the converged stationary beam with a strip detector, in which case one would instantaneously integrate over the



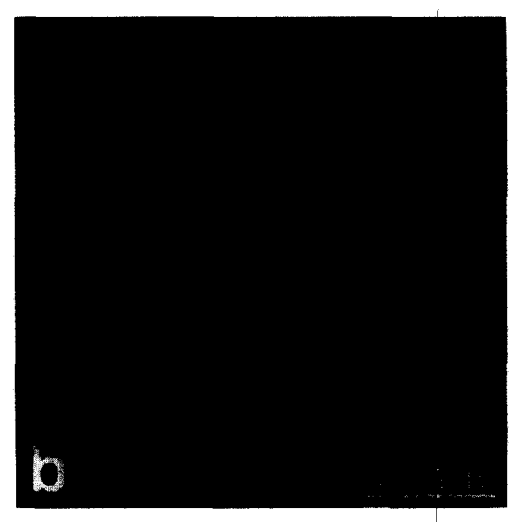


Fig. 2. (a) Multiple exposure diffraction pattern (reverse contrast) of a twinned region in the Terfenol-D thin foil. A converged beam was used to illuminate the sample, and each disk corresponds to an increasingly larger beam tilt angle. The directions of the translations of the diffraction disk determine the relative orientation of the beam tilts with respect to the twin plane and hence the crystallographic reference frame of the sample. (b) Foucault image of the region corresponding to the diffraction pattern in (a). The beam tilt directions U and V are indicated with respect to the twin plane.

beam tilt. For a fixed aperture one can simulate the strip detector by adding the images for increasing beam tilts (assuming there is no image shift at any beam tilt) and one obtains four summed images,  $\Sigma_{+U}$ ,  $\Sigma_{-U}$ ,  $\Sigma_{+V}$ , and  $\Sigma_{-V}$ . The difference between the  $\Sigma_{+U}$  and  $\Sigma_{-U}$  sums is then proportional to the magnetic induction component in the +U direction (this difference image is equivalent to the difference current between sectors of the quadrant detector in the DPC-STEM technique). The information required to produce an induction map are four series of Foucault images, taken for tilts in the  $\pm U$  and  $\pm V$  directions, along with the U and V tilt directions relative to the crystallographic directions in the sample.

For the experimental setup used in this paper (JEOL 4000EX+GIF) the mapping method is implemented as follows: the JEOL 4000EX has two sets of image shift coils which can be used in conjunction to provide a post-specimen beam tilt. The first image shift coils which sit just above the objective minilens coil provide the beam tilt. The accompanying shift of the image can be compensated for in large part by the second set of image shift coils, which sit just below the objective minilens. For the observations presented in this paper, the currents in both sets of image shift coils were set manually, resulting in small image shifts from one beam tilt to the next. These shifts can be compensated for in the image processing stage of the analysis.

The determination of the direction of the tilt relative to the crystallographic reference frame of the sample is a simple matter and can be accomplished by recording a long exposure diffraction pattern while simultaneously tilting first in the +U direction and then in the +V direction. The only other information required to determine the beam tilt directions is then the angle of rotation between the diffraction pattern and the image at a given magnification. As most of Terfenol's more interesting domain features occur near twin boundaries, we have found it convenient to record diffraction patterns across

twin boundaries, which can then be overlaid directly onto the image. A reverse-contrast example is shown in Fig. 2(a); the transmitted beam was originally centered on the negative. The tilt directions are shown in Fig. 2(a) and by rotating 90° clockwise the corresponding magnetization directions can be determined. This procedure establishes the angle between the tilt directions and the twin plane. A bright field (or dark field) image of the twin region can then be used to determine the relative orientation of tilt directions and the image frame. Fig. 2(b) is a Foucault image of a twin boundary near the region shown in Fig. 1 showing the induction directions.

# **INDUCTION MAPPING RESULTS**

Figure 3 shows four series of zero-loss Foucault images (slit width 15 eV) for the tilt directions derived in the previous section. The tilt angle was increased up to the maximum value, at which point most Foucault contrast disappeared from the image. Ideally one would tilt to an angle corresponding to the case where the diffraction disk no longer falls on the SA aperture. Unfiltered images were obtained under identical conditions except for the removal of the energy slit in order to investigate the effect of energy filtering. The Foucault images in each series were aligned using an interactive program and then summed on a per-pixel basis. The sums for the filtered series are shown in Fig. 4, along with the difference maps for both the filtered and unfiltered series. The  $B_U$  and  $B_V$  directions, derived from Fig. 2(b) are also indicated on the figure. The difference maps (typically 512 × 512 pixel images) can then be rebinned and displayed as a vector map, shown in Fig. 5 for both the filtered and unfiltered case. Note that there are only minor differences between the two vectormaps, mostly near the domain walls, so that the use of

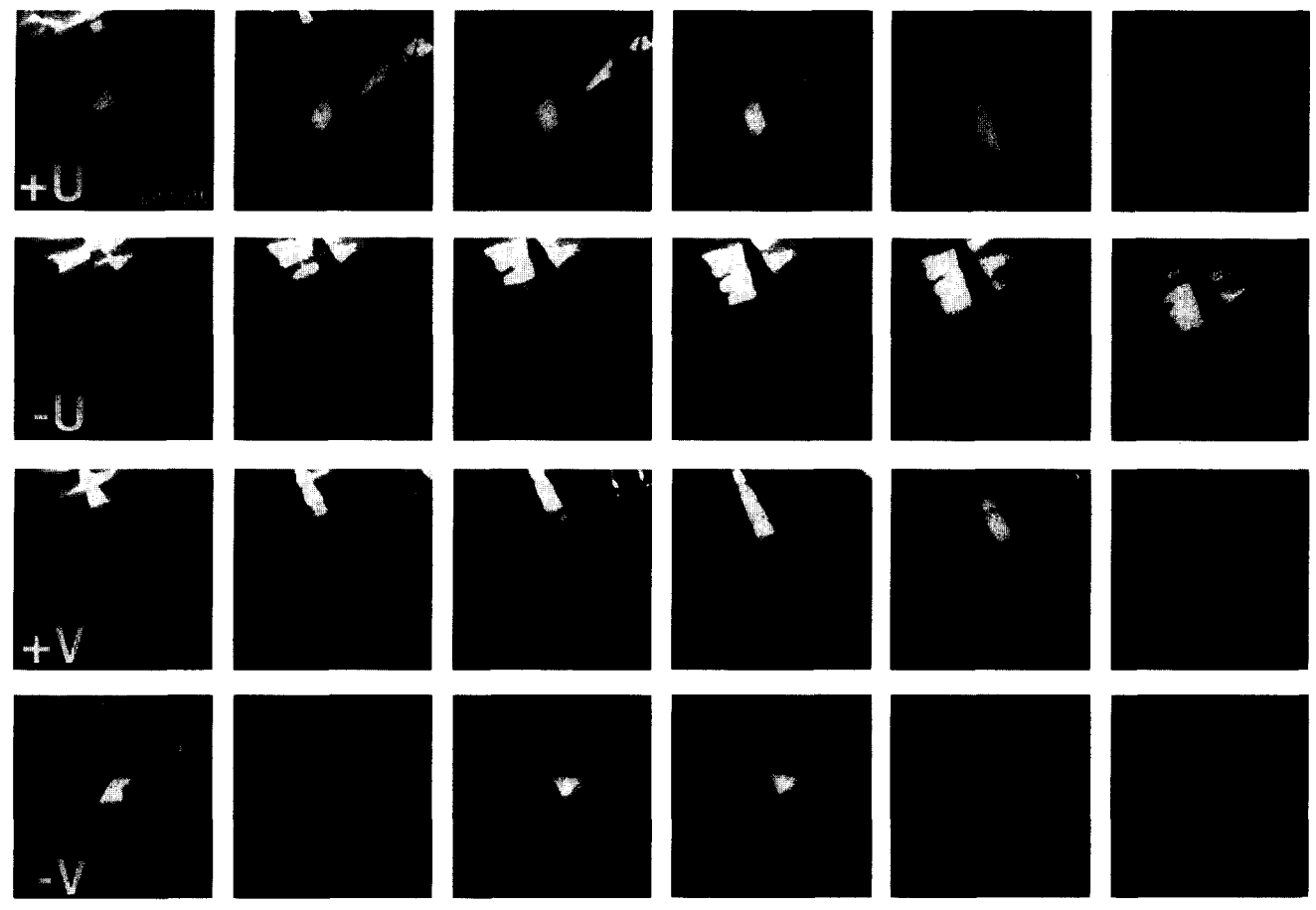


Fig. 3. Beam tilt Foucault series for the  $\pm U$  and  $\pm V$  tilt directions. The beam tilt was increased until no more Foucault contrast could be observed.

zero-loss filtering appears to have only a small effect. This will be further addressed in the Discussion section.

A quantitative analysis of the induction maps obtained by this technique is only possible if one can also model the induction mapping process. A detailed account of such a simulation algorithm together with examples of simulated induction maps is presented in the following section.

# LORENTZ IMAGE SIMULATIONS

The Aharonov-Bohm phase shift

Both Fresnel and Foucault images can be simulated using an algorithm first proposed by Mansuripur (1991). In Dooley and De Graef (1997) we have presented preliminary results of image simulations for a particular domain configuration in Terfenol-D. We obtained good qualitative agreement between experimental zero-loss Fresnel and Foucault images, and the corresponding simulated images. Here we extend the simulation method to include magnetic induction mapping.

Since a ferromagnetic thin foil can be regarded as a strong phase object, magnetic contrast image simulations are rather similar to standard high resolution simulations. One first computes the phase shift imparted on the beam electrons by the Aharonov-Bohm

(Aharonov and Bohm, 1959) or A–B effect (taking into account the proper incident beam direction), then one multiplies the Fourier transform of the wave function by the contrast transfer function (which includes aperture truncation, defocus, spherical aberration and attenuation components), and the image intensity is then given by the modulus squared of the inverse Fourier transform. The A–B phase shift is most easily computed when one assumes a periodic two-dimensional magnetic unit cell, e.g. a periodic arrangement of 180° and 71° domain walls in Terfenol-D.

If the discrete Fourier components of the magnetic induction over a unit cell of  $P \times Q$  pixels with pixel spacing D are represented by  $\overrightarrow{M}_{mn}$ , with m=1,...,P and n=1,...,Q, then the A-B phase shift is given by the discrete two-dimensional Fourier transform (Mansuripur, 1991):

$$\Phi(x,y) = \frac{2\pi e}{h} \sum_{m=0}^{P} \sum_{n=0}^{Q} i \frac{t}{|\vec{k}|} G_{\vec{p}}(t,\vec{k}') (\hat{k} \times \hat{z}) \cdot (\vec{p} \times (\vec{p} \times \vec{M}_{mn})) e^{2\pi i \left(\frac{mx}{P} + \frac{ny}{Q}\right)}$$
(1)

where the prime on the summation indicates that the term (m, n)=(0,0) does not contribute to the summation,  $\overrightarrow{k}=ue_x^*+v\overrightarrow{e}_y^*$  is the frequency vector,  $\overrightarrow{e}_x^*$  and  $\overrightarrow{e}_y^*$  are the reciprocal unit vectors,  $\overrightarrow{p}$  is the beam direction expressed in the orthonormal reference frame, t is the

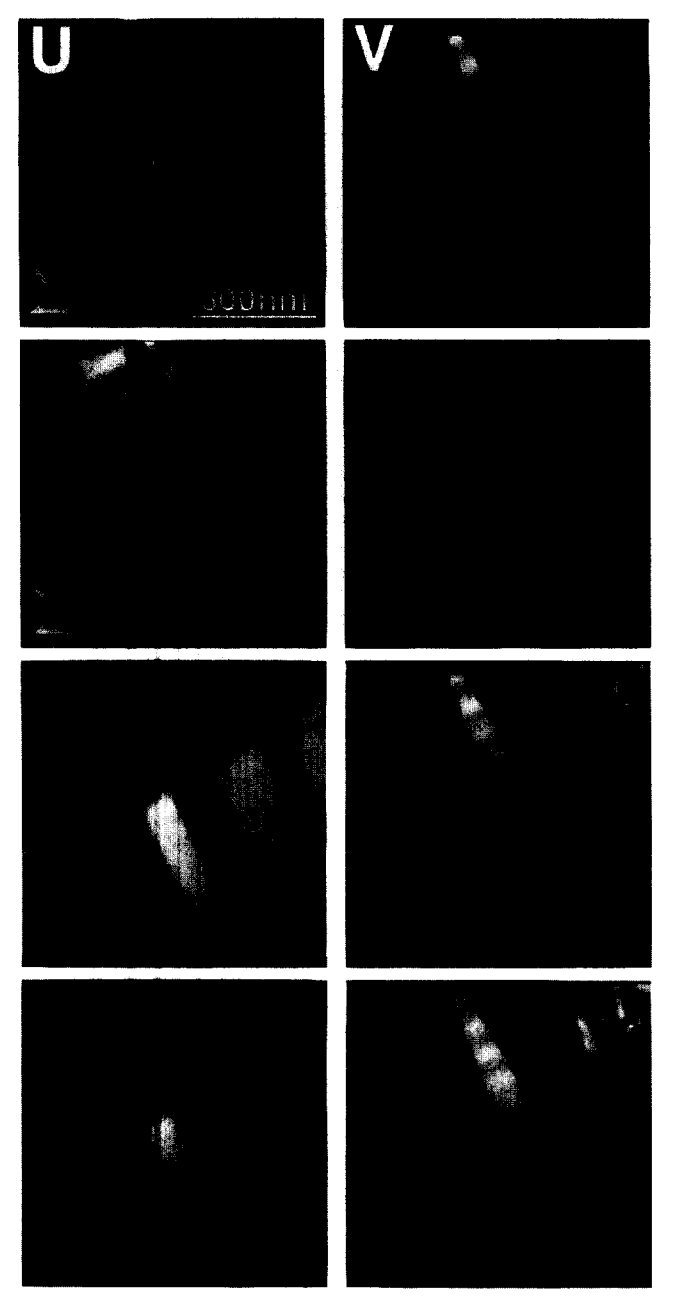


Fig. 4. The top two rows show summed images for the four tilt series of the previous figure. The bottom two rows show the difference images  $\Sigma_+$ - $\Sigma_-$  for both tilt directions, for the zeroloss and unfiltered tilt series. The linear features near the edges of those images are artifacts of the image alignment procedure.

sample thickness, a  $^{\wedge}$  indicates unit vectors, and  $G_{\overrightarrow{p}}(t, \overrightarrow{k})$  is given by:

$$G_{\overrightarrow{p}}(t,\overrightarrow{k}) = \frac{1}{(\overrightarrow{p} \cdot \hat{k})^2 + (\overrightarrow{p} \cdot \hat{z})^2} \frac{\sin\left(2\pi t \frac{\overrightarrow{p} \cdot \overrightarrow{k}}{\overrightarrow{p} \cdot \hat{z}}\right)}{2\pi t \frac{\overrightarrow{p} \cdot \overrightarrow{k}}{\overrightarrow{p} \cdot \hat{z}}}$$
(2)

For normal beam incidence  $(p||\overrightarrow{z})$  the function  $G_p^{\rightarrow}(t, \overrightarrow{k})$  takes on the value 1. Implementation of this equation is straightforward and, using Fast Fourier Transforms for a  $512 \times 512$  array, takes less than 30 s on

# **Magnetic Induction Maps**

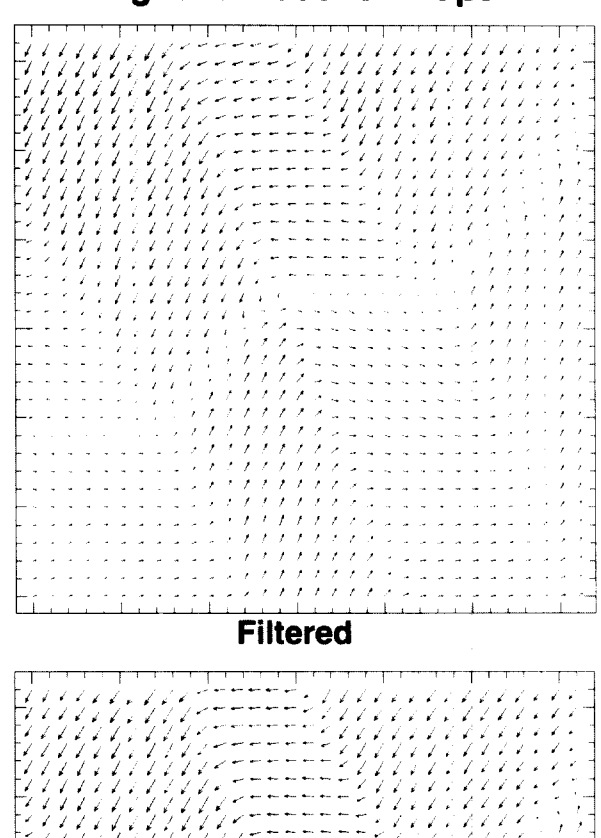


# Fig. 5. In-plane magnetic induction vector maps for the central area of the difference images of the previous figure, for both the zero-loss and unfiltered mapping experiments.

Unfiltered

a DEC AlphaStation 200. Note that the (m,n)=(0,0) term does not contribute to the phase shift in equation (1); the meaning of this will be further addressed in the Discussion section.

The resulting wave function is given by

$$\psi(\overrightarrow{r}) = e^{i\left(\frac{2\pi}{r}\overrightarrow{p}\cdot\overrightarrow{r} + \phi(\overrightarrow{r})\right)}$$
 (3)

or in the back focal plane of the objective (mini) lens

$$\Psi(u,v) = \mathcal{F}_{u,v}[\psi(x,y)] \{ a(u,v) e^{-i\pi\lambda \Delta f(u^2+v^2)} e^{-(\pi\theta_c \Delta f)^2(u^2+v^2)} \}$$
 (4)

with  $\mathcal{F}_{u,v}$  being the direct Fourier transform operator, u and v the spatial frequency coordinates in the back focal

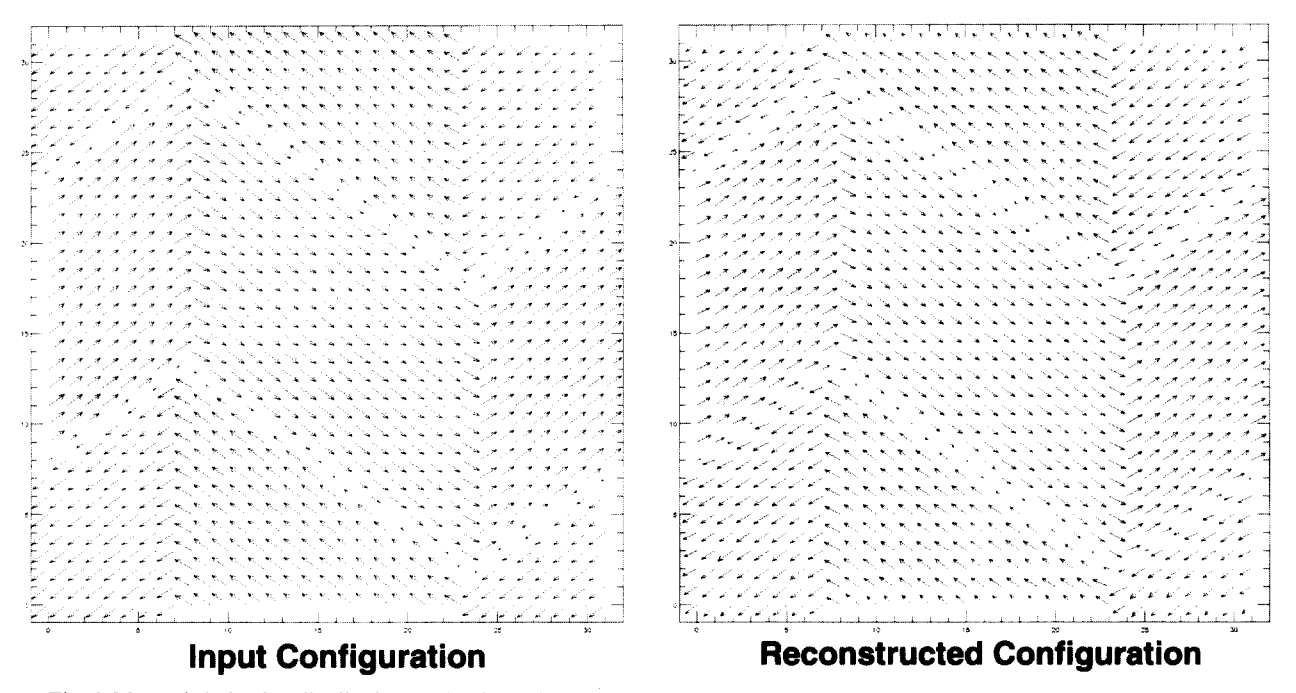


Fig. 6. Magnetic induction distribution used as input for the model simulations. This particular domain configuration is frequently found in Terfenol-D thin foils. On the right the reconstructed vector map is shown (see text for details).

plane, a(u,v) the aperture function,  $\Delta f$  the defocus, and  $\lambda$  the electron wavelength. Note that the spherical aberration contribution to the transfer function has been ignored in the above expression. This is a good approximation since for a Lorentz deflection angle of 40  $\mu$ rad the beam phase shift caused by spherical aberration ( $C_s$ =120 mm for the objective minilens of the topentry JEOL 4000EX) is  $\Delta \chi = \frac{2\pi}{\lambda} \frac{C_b \theta^4}{4} = 0.29 \,\mu$ rad, negligible compared to the phase shifts induced by the A–B effect.

The image intensity is as usual given by (ignoring image rotation and magnification)

$$I(x,y)=|\mathcal{F}^{-1}_{x,y}[\boldsymbol{\varPsi}(u,v))|^2$$
 (5

For Foucault imaging the defocus  $\Delta f$  is set equal to zero, so that the image contrast is mostly determined by the diffraction aperture and the beam divergence angle  $\theta_c$ . Magnetic induction image simulations can now be performed by tilting the beam in two orthogonal directions U and V, which is accomplished by changing the vector  $\overrightarrow{p}$  in equation (3). The range of vectors  $\overrightarrow{p}$  to be included in the simulation is determined by the divergence angle  $\theta_c$  of the incident beam and the Lorentz deflection angle.

# Simulation of magnetic induction maps

We will illustrate induction mapping simulations by means of an example. Consider the magnetic induction configuration shown on the left of Fig. 6. It is defined on a grid of  $512 \times 512$  pixels, with a length scale of 1 nm per pixel. There are two sets of domain walls: the vertical walls correspond to  $71^{\circ}$  domain walls and are described

by a sinusoidal profile and a width of 10 nm. The second set of zig-zag walls are of the 180° Bloch wall type with a width of 16 nm. The upper half of this particular domain configuration should be compared with the central region of the experimental induction map in Fig. 3. The bulk domain wall widths calculated in Clarke and Tanner (1982) are of the order of 50–150 nm. As the sample becomes thinner the domain wall width decreases. Little is known about the thickness of domain walls in thin films of Terfenol-D and to the authors' knowledge no direct measurements have been made. For the simulations in this paper we have selected a domain wall width of 16 nm.

Simulations are performed for a saturation magnetization of 1 Tesla, a foil thickness of 100 nm, and an incident beam energy of 400 keV (wavelength  $\lambda$ =1.644 pm). The beam tilt can be varied by changing the beam direction represented by the normalized vector  $\overrightarrow{p}$  along predefined directions. To allow for a comparison between the set of experimental images shown in the previous sections and the computed images, the simulation tilt directions are chosen to correspond to the experimental directions. The beam direction  $\overrightarrow{p}$  hence varies along one of the two directions

$$\overrightarrow{t}_{\pm U} = \pm (\cos \alpha \overrightarrow{t}_{[011]} - \sin \alpha \overrightarrow{t}_{[100]})$$

$$\overrightarrow{t}_{\pm V} = \pm \left(\sin a \overrightarrow{t}_{[011]} + \cos a \overrightarrow{t}_{[100]}\right)$$

where a is the angle between the [011] direction and the +U tilt direction ( $a=-216.8^{\circ}$  for the mapping in Figs 3-5). As the beam is tilted away from normal incidence, it becomes sensitive to the components of magnetization in the  $\hat{z}$  direction.

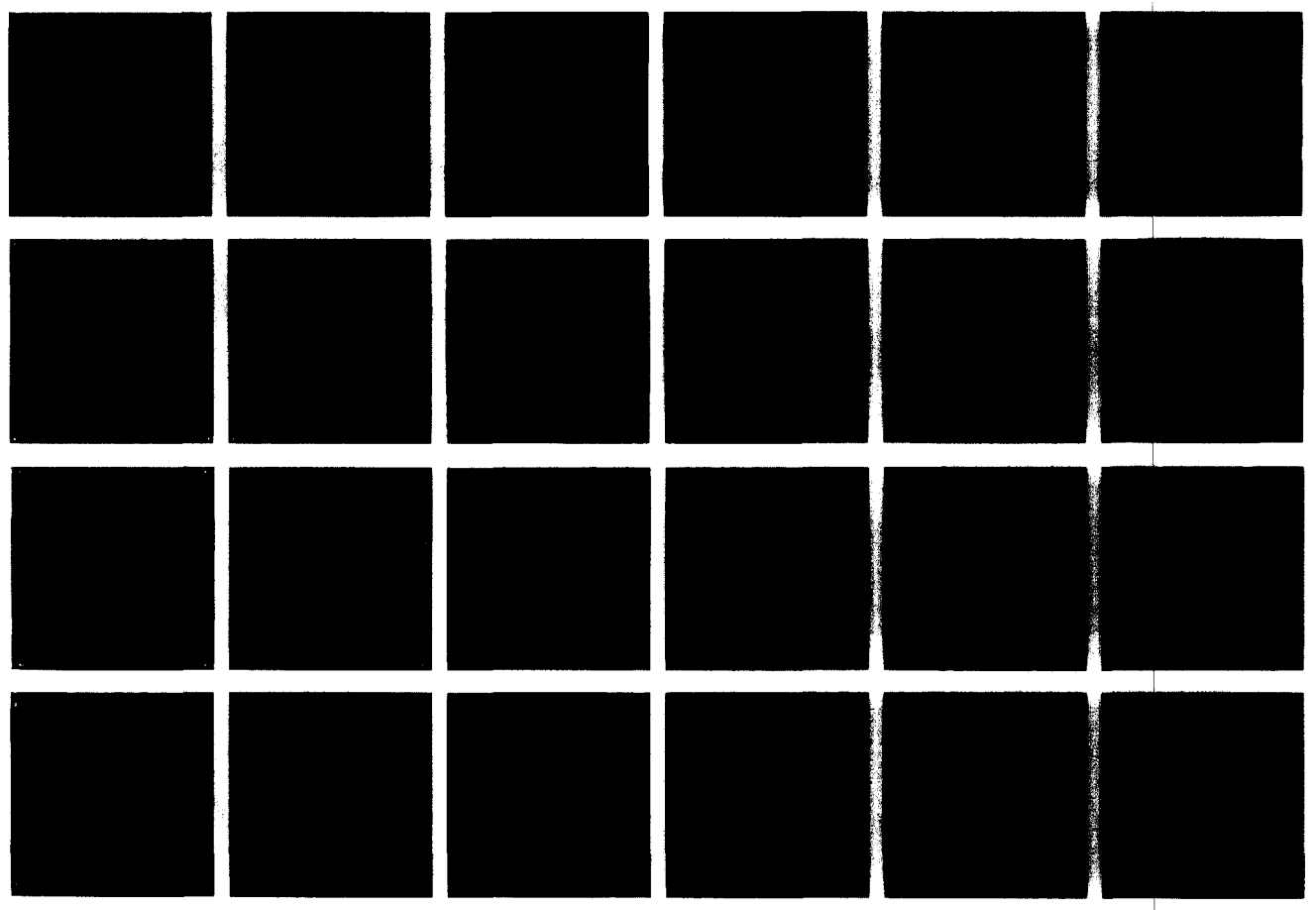


Fig. 7. Simulated tiltseries for the  $\pm U$  and  $\pm V$  tilt directions. Simulation conditions are discussed in detail in the text.

Tilt series were simulated for 20 tilt steps in each direction, for a beam divergence angle  $\theta_{\rm c}$ =1 mrad, a beam tilt increment of 3.5  $\mu$ rad, and an aperture radius of 0.05 nm<sup>-1</sup>. Figure 7 shows a portion of the complete tilt series, for tilt increments between neighboring images of 10.5  $\mu$ rad. Note that the images contain a large number of fringes parallel to the domain walls; these fringes are caused by coherent interference between electrons scattered by the neighboring domains, and depend in a sensitive way on the exact beam tilt. Since image intensities are added incoherently to obtain the summed tilt series, the effect of individual sets of fringes is washed out in the final sums.

The summed series (for 20 beam tilts) are shown in the top two rows of Fig. 8. Note the presence of a bright fringe at the location of the 180° domain wall in the  $\pm U$  sums. In the experimental summed tilt images such a fringe is only observed for the zero-loss acquisitions, not for the unfiltered images, as is illustrated in Fig. 9. This sum was obtained for a sample region similar to that shown in Fig. 1, for a total number of seven beam tilts in the  $\pm U$  direction. It is clear that the fringe is only present in the zero-loss image, which indicates the need for energy filtering as part of the induction mapping technique. In addition, the background intensity of the summed images is different for the filtered and unfiltered images, and since the in-plane magnetic induction components are proportional to the intensity in the differ-

ence image we must discard the unfiltered induction maps as potentially unreliable.

The difference images in Fig. 8 should be compared with the experimental difference images in Fig. 4: the top half of the simulated images corresponds with the central 180° domain wall in the experimental images. We found a good qualitative agreement between these sets of images, including the presence of a faint bright fringe in the experimental  $\pm U$  sums. The reconstructed vector map is shown on the right of Fig. 6 and can be directly compared with the input structure.

The vector map shows reasonable qualitative agreement between the reconstructed and input patterns. A more quantitative comparison can be made regarding the domain wall profiles. Figure 10 shows the input profile of the induction component parallel to the 16-nm-wide 180° domain wall (thick line) together with the reconstructed profiles for three different diffraction aperture radii, 0.05, 0.025 and 0.0125 nm <sup>-1</sup>. The resolution of the magnetic induction mapping technique depends in a sensitive way on two independent quantities: (1) the aperture radius; and (2) the relative orientation of the beam tilt direction with respect to the domain wall.

As the aperture radius is decreased with respect to the diffraction disk radius, the aperture will better approximate an ideal strip detector and one expects a perfect reconstruction for an infinitely narrow strip detector (or

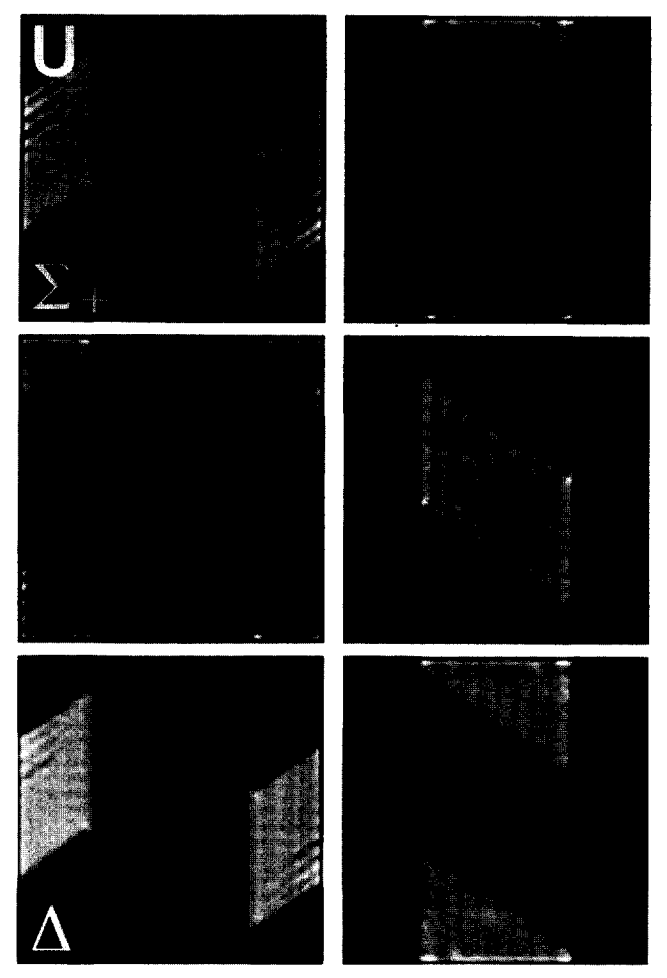


Fig. 8. The top two rows show the sum images for 20 beam tilts for each tilt direction. The bottom row shows the difference images which are proportional to the in-plane magnetic induction components.

infinitely narrow aperture). In practice this is limited by the available intensity and there will be a minimal aperture radius below which the intensity in the image drops below the noise level. If the aperture radius is taken to be comparable to or larger than the radius of the diffraction disk, then all directional information is simultaneously present in the Foucault image series, and hence a reconstruction of the domain wall profile will fail. We thus conclude that there is an optimum aperture radius, which for the simulations in this paper must lie between 0.0125 and 0.05 nm<sup>-1</sup> (according to Fig. 10).

The reciprocal space information related to the domain wall profile is located along the line perpendicular to the domain wall. If the beam tilt direction coincides with the domain wall normal, then one will sample all frequency components of the wall profile, and an accurate reconstruction will be possible. However, if the tilt direction deviates from the wall normal, then the reconstructed wall profile will show decreasing agreement with the input profile for a decreasing aperture radius. Refinements of this method to determine the domain wall width are currently being analyzed and will be discussed in a forthcoming paper.

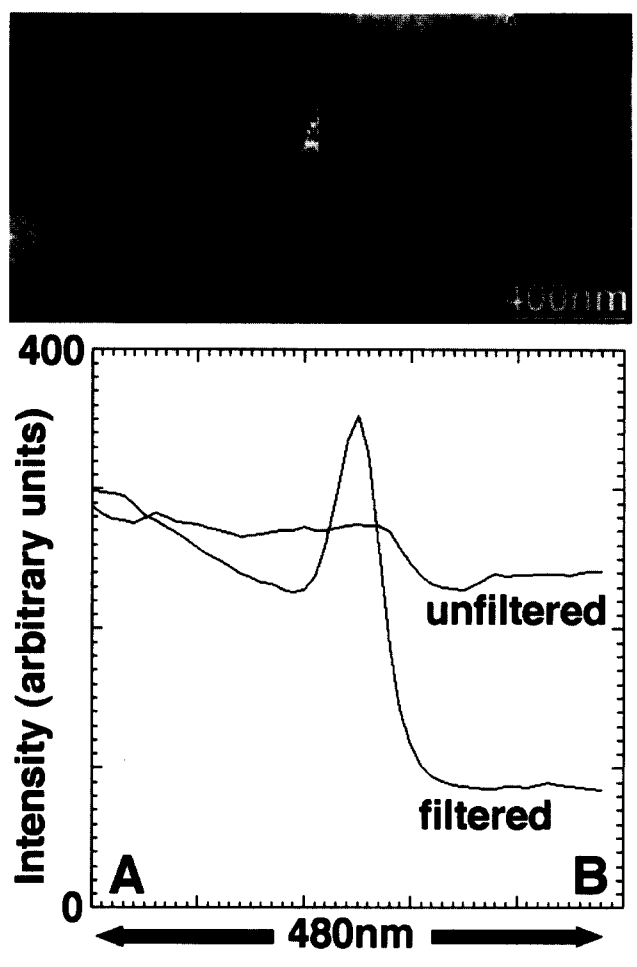


Fig. 9. Illustration of the effect of zero-loss energy filtering on the summed tilt images. The image in the left (a sum for seven beam tilts) shows no fringe at the domain wall, whereas the one on the right (for a slit width of 15 eV) shows a clearly defined fringe, in good qualitative agreement with the simulation results.

# DISCUSSION AND CONCLUSIONS

Although the advantages of energy filtering may appear to be small in the case of Terfenol-D, zero-loss filtering will undoubtedly be required for magnetic mapping studies of materials with a smaller saturation magnetization. The large magnetization of Terfenol-D leads to relatively large splitting of the central beam, and hence strong Foucault contrast. Zero-loss filtering improves the signal to noise ratio in the images, but when the Foucault signal is already very strong, this improvement is less critical than when it is weak.

Since the Lorentz deflection angle is proportional to the sample thickness one must use a sample with nearly constant thickness across the region of interest to perform accurate magnetic induction mapping experiments. For a wedge shaped crystal, electrons which travel through the thicker part of the wedge will have a higher probability of undergoing inelastic scattering events, and will also experience a larger Lorentz deflection. The induction mapping technique produces information which is proportional to the product of the in-plane components of the magnetic induction and the sample thickness, and consequently irregularities in the sample

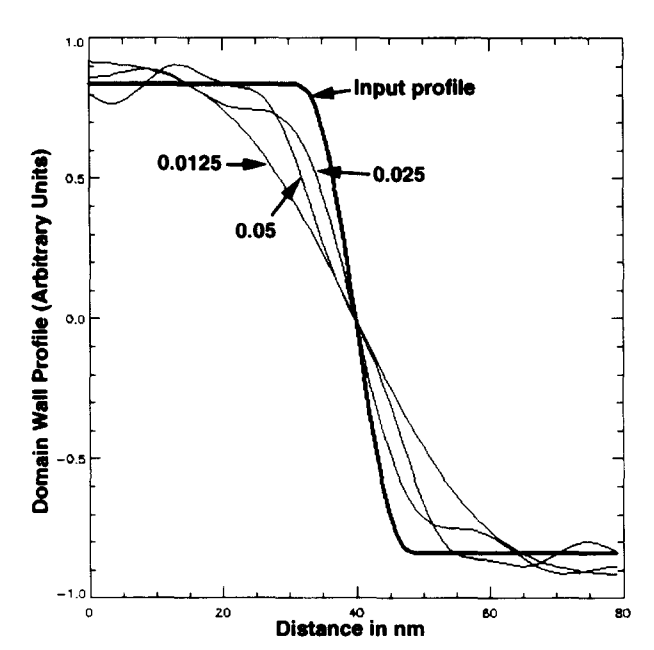


Fig. 10. Comparison of the reconstructed magnetic induction component parallel to the 180° domain wall with the input profile (thick line, domain wall width 16 nm); the reconstructed profiles used aperture radii of 0.0125, 0.025 and 0.05 nm<sup>-1</sup>, respectively. Note that the profile for 0.025 nm<sup>-1</sup> shows the best agreement with the input profile.

thickness may cause artifacts in the induction maps. One must also take care to orient the sample such that there is only negligible diffraction contrast. This is particularly important if quantitative comparisons with simulated images (which are based on a pure strong phase object) are needed.

It is important to note that the Mansuripur expression for the A-B phase shift does not include a DC component [the term (m,n)=(0,0) does not contribute to the summation]. This is a consequence of the fact that the origin of the reference frame was chosen to be at the center of the foil, and since the DC component is an odd function of z the bottom half of the foil cancels the DC phase changes introduced by the top half. In practice this means that the reconstruction method based on the Mansuripur algorithm cannot detect the DC component of the magnetic induction. For this reason it is necessary to rescale the zero-loss U and V difference maps such that the average components are equal to zero. This is not a real limitation since the magnetic induction mapping technique, as described in this paper and in Daykin and Petford-Long (1995), is a relative technique: one measures changes in the in-plane magnetic induction components relative to a reference configuration which is obtained by moving the sample out of the beam and centering the beam in the back focal plane aperture. If a sample has a DC component of the magnetization (or equivalently, a translation in the diffraction pattern), then it is not clear a priori whether this component is due to the actual domain configuration or to fringe fields. For the material discussed in this paper, Terfenol-D, the rods from which TEM foils were prepared were demagnetized before sample preparation, and hence the average magnetic induction over a sufficiently large volume may be taken equal to zero. Comparison of experimental induction maps with model calculations using the Mansuripur algorithm are hence only meaningful if the DC component is subtracted from the experimental maps.

In its current implementation the Mansuripur algorithm does not take into account a z-variation of the magnetic induction in the sample. In particular, fringe fields are completely ignored. The algorithm does lend itself to implementations in a multi-slice framework, where one could include variations of the magnetic induction along the z-direction. One important application of such simulations may be in the area of magnetic recording materials, where one has analytical models for the fringe fields near the recording surface. A more complete discussion of a multi-slice implementation of magnetic image simulations will appear in a forthcoming publication.

As mentioned in the previous section, the resolution of the magnetic induction mapping technique depends in a sensitive way on the radius of the diffraction aperture and the relative orientation of the tilt directions and the magnetic domain walls. Since the beam tilts used for the experiments in this paper were all performed through manual changes of the image shift coil currents, it was impractical to attempt to combine the doils in such a way that the beam tilts would be in directions orthogonal to the domain walls. Therefore, the aperture radius should not be so small that the center of the diffraction disk(s) does not pass through it for any of the beam tilts used. If the mapping technique were fully automated, then the image shift coil currents could be changed so that the beam tilt directions coincide with the Lorentz deflection directions, in which case the highest resolution induction maps may be acquired. Unless the angle between the tilt direction and the domain wall normal is minimized, the mapping technique will always overestimate the domain wall width.

In summary, we have presented a detailed account of an energy filtered magnetic induction mapping technique in the TEM, which allows for the acquisition of high resolution maps of the in-plane magnetic induction in a thin foil. We have used Terfenol-D to illustrate the experimental method. Detailed image simulations of the mapping results were carried out using an algorithm first suggested by Mansuripur and results of the simulations are in good agreement with experimental observations.

Acknowledgements—The authors would like to thank N.T. Nuhfer for stimulating discussions, and N. Biery for providing the image alignment procedure used to compensate for image shifts during beam tilting. This work was supported in part by the National Science Foundation through contract No. DMR-9403621 under the guidance of Dr L. Inglehart.

## REFERENCES

Aharonov, Y. and Bohm, D., 1959. Significance of electromagnetic potentials in the quantum theory. *Phys. Rev.*, **115**, 485–491.

- Al-Jiboory, M. and Lord, D., 1990. Study of the magnetostrictive distortion in single crystal Terfenol-D by x-ray diffraction. *IEEE Trans. Magn.*, 26, 2583–2588.
- Chapman, J. N., Batson, P. E., Waddell, E. M. and Ferrier, R. P., 1978. The direct determination of magnetic domain wall profiles by differential phase contrast electron microscopy. *Ultramicroscopy*, 3, 203-214.
- Clark, G. F., Tanner, B. K. and Savage, H. T., 1982. Synchrotron X-radiation topography studies of the magnetization process in Tb<sub>0.27</sub>Dy<sub>0.73</sub>Fe<sub>2</sub>. *Philos. Mag. B*, 46, 331–343.
- Daykin, A. and Petford-Long, A., 1995. Quantitative mapping of the magnetic induction distribution using Foucault images formed in a transmission electron microscope. *Ultramicroscopy*, 58, 365-380.
- Dooley, J. and De Graef, M., 1997. Energy filtered Lorentz microscopy. *Ultramicroscopy*, **67**, 113–131.
- Huang, M. Q., Zheng, Y. and Wallace, W. E., 1994. SmCo (2:17-type) magnets with high contents of Fe and light rare earths. J. Appl. Phys., 75, 6280-6282.
- James, R. and Kinderlehrer, D., 1993. Theory of magnetostriction with applications to Tb<sub>x</sub>Dy<sub>1-x</sub>Fe<sub>2</sub>. *Phil. Mag. B*, **68**, 237-274.
- Lord, D., Savage, H. and Rosemeier, R., 1982. X-ray topography observation of a DyTbFe crystal. J. Magn. Magn. Mat., 29, 137-140.
- Mansuripur, M., 1991. Computation of electron diffraction patterns in Lorentz electron microscopy of this magnetic films. *J. Appl. Phys.*, **69**, 2455–2464.
- Reimer, L., 1993. Transmission Electron Microscopy, Springer, Berlin.